Published in final edited form as:

MAGMA. 2018 June ; 31(3): 355–366. doi:10.1007/s10334-017-0657-5.

Manipulating transmit and receive sensitivities of radiofrequency surface coils using shielded and unshielded high-permittivity materials

M. V. Vaidya[1,2,3], **C. M Deniz**[1,2,3], **C. M. Collins**[1,2,3], **D. K. Sodickson**[1,2,3], and **R. Lattanzi**[1,2,3]

[1]Center for Advanced Imaging Innovation and Research (CAI[2]R) and Bernard and Irene Schwartz Center for Biomedical Imaging, Department of Radiology, New York University School of Medicine, 660 1st Ave. New York, NY 10016 USA

[2]The Sackler Institute of Graduate Biomedical Sciences, New York University School of Medicine550 First Avenue, New York, NY 10016 USA

[3]NYU WIRELESS, Polytechnic Institute of New York University, 2 Metro Tech Center, Brooklyn, NY 11201 USA

Abstract

OBJECT—To use high permittivity materials (HPM) positioned near radiofrequency (RF) surface coils to manipulate transmit/receive field patterns.

MATERIALS AND METHODS—A large HPM pad was placed below the RF coil to extend the field-of-view (FOV). The resulting signal-to-noise (SNR) was compared to the performance of other coil configurations covering the same FOV in simulations and experiments at 7T. Transmit/receive efficiency was evaluated when HPM discs with or without a partial shield were positioned at a distance from the coil. Finally, we evaluated the improvement in transmit homogeneity for a four-channel array with HPM discs interposed between adjacent coil elements.

RESULTS—Various configurations of HPM improved SNR, transmit/receive efficiency, extended the excitation/reception sensitivity overlap and FOV when positioned near a surface coil. For a four channel array driven in quadrature, shielded HPM discs enhanced the field below the discs as well as at the center of the sample as compared to other configurations with or without unshielded HPM.

CORRESPONDING AUTHOR: Manushka Vaidya, The Bernard and Irene Schwartz Center for Biomedical Imaging, New York University Langone Medical Center, 660 First Avenue – Fourth Floor, New York, NY 10016, USA, manushka.vaidya@nyumc.org.

CONFLICT OF INTEREST

The authors declare that they have no conflict of interest.

AUTHORS' CONTRIBUTION

Vaidya: This author was involved in protocol/project development, data collection, and data analysis.
Deniz: The author was involved in data collection and analysis.
Collins: The author was involved in protocol/project development.
Sodickson: The author was involved in protocol/project development.
Lattanzi: The author was involved in protocol/project development.

CONCLUSION—Strategically positioning HPM at a distance from a surface coil or array can increase the overlap between excitation/reception sensitivities, and extend the FOV of a single coil for reducing the number of channels in an array while minimally affecting the SNR.

Keywords

High permittivity materials; RF shields; Magnetic Resonance Imaging; passive shimming; B_1 field patterns; electromagnetic field simulations; ultra-high-field MRI

INTRODUCTION

Radiofrequency (RF) inhomogeneity can severely degrade image quality and diagnostic information for magnetic resonance imaging (MRI) applications at ultra-high field (UHF) (> 4T) [1–3]. One cause of the inhomogeneous field distribution is that the wavelength of the applied magnetic field ($\boldsymbol{B}_1$) at high operating frequencies is comparable to the size of the imaging body, causing constructive and destructive interferences as it propagates within the sample [4–10]. Multiple channel MR excitation techniques, such as RF shimming [11–13] and parallel transmission [14–16], have been proposed to improve $\boldsymbol{B}_1$ homogeneity. For example, in analytical simulations it was shown that parallel transmission could achieve perfect homogeneity on a plane [16]. Such techniques, however, are practically limited by the number of available independent transmit channels and escalating costs for systems with a greater number of channels.

On the other hand, a larger number of receive channels is usually available and desirable in modern MR scanners, since simulation studies have shown that a large number of coils may be required to approach the ultimate intrinsic signal to noise ratio (UISNR), which is the highest possible SNR consistent with electrodynamics, at the center of an object. The number of coils can approach 128 for a body-size [17] object and 32 for a head-size object [18,19]. As a result of this mismatch between the number of available channels and due to different needs of transmit and receive arrays, these arrays are often separately constructed and independently optimized to maximize transmit homogeneity and SNR [20,21]. Because these designs are complex and require multiple detuning circuits, a single array aimed at both transmission and signal reception, with some compromise on the number of optimal channels is sometimes pursued as a practical alternative. However, optimization of such an array can be challenging, since transmit and receive sensitivities of the same surface coil do not overlap completely, especially at UHF, reducing the overall imaging efficiency [22,23].

Using high permittivity materials (HPMs), originally in the form of bags of water, between a volume coil and the sample was proposed to reduce $\boldsymbol{B}_1$ inhomogeneity at high field strength [24,25]. The advantage of this method was that it required no additional electronics; however, the large sized bags required for this purpose are not optimal for tight-fitting coils. More recently flexible HPM pads with a relative permittivity greater than water ($\varepsilon_r = 80$), such as a slurry of calcium titanate powder and water ($\varepsilon_r = 110$) [26] or of barium titanate powder or beads and water ($\varepsilon_r = 150–500$) [27,28], have been used to further improve coil performance with geometries that can be easily incorporated into existing coils. The beneficial effects of HPMs have been attributed to displacement currents induced within the

HPM, which create additional magnetic fields that enhance $\boldsymbol{B}_1$ within the imaging sample and improve transmit efficiency, SNR, and excitation homogeneity [25,29–31]. A variety of studies, subsequently, have demonstrated the benefit of using HPMs for in-vivo applications [32–40]. Some published studies focused on increasing transmit efficiency of a volume coil using HPM [26], while others used HPMs to increase the SNR performance of surface coils [41,30]. In previous work, HPMs were placed either between the coil and the sample [25–27,29–31], or between the coil and the RF shield [42].

In this work, we investigate the use of HPMs positioned at a distance from a surface coil to extend the transmit and receive field-of-view (FOV) in order to potentially reduce the number of array elements without compromising overall imaging performance. This work also aimed at using HPM for improving the overlap of the transmit and receive sensitivity distribution of surface coils, to enable efficient excitation and reception with the same element at UHF.

MATERIALS AND METHODS

Experiments

Experiments were performed to evaluate whether HPM pads could extend the FOV of surface coils. In particular, we compared the SNR performance of a small surface coil placed with a single large HPM (Fig. 1A) with other configurations: a three-element array and a single large surface coil both covering the same FOV, and the small coil without the HPM pad (Fig 2). A cylindrical phantom (Fig 2A) was constructed and filled with a solution of sugar, NaCl and distilled water [43] to obtain tissue-like electrical properties of $\varepsilon_r = 61.8$, $\sigma = 0.87$ S/m, confirmed with a dielectric probe (85070E Dielectric Probe Kit, Agilent Technologies). Benzoic acid was added to the solution as a preservative. All coils were positioned at a distance of 25 mm from the surface of the cylindrical phantom. An HPM mixture was created with Barium titanate powder (Sigma Aldrich, 99 %, powder, < 3 μm) and deuterium oxide (Sigma Aldrich, 99 atom %D) to form a saturated slurry with properties $\varepsilon_r = 297$ and $\sigma = 0.38$ S/m [27,28]. The mixture was then poured into a plastic bag, which was sealed to form a large HPM pad (Fig 2A).

All coils were constructed on a former approximating the curvature of the phantom, and were tuned to 297.2 MHz and matched to 50 Ohms (S_{11}<−20dB). For the three-element array, the neighboring elements were geometrically decoupled (S_{21}<−10dB). The poor decoupling was likely due to the presence of a gap between the phantom and the coils, which limited coupling with the phantom, resulting in higher coupling between neighboring elements. The size of this gap was chosen to accommodate the HPM pad and kept constant for all coil configurations (Fig. 1). Experiments were carried out on a whole-body 7T scanner (MAGNETOM, Siemens Healthineers, Erlangen, Germany). For the three-element array, a parallel transmission system was used to adjust the phases of the individual coils such that the excitation fields constructively combined at the center of a transverse slice. Flip-angle maps were obtained using a pre-saturation based turbo-FLASH imaging technique [44]. SNR maps were calculated using the raw data from two gradient echo (GRE) acquisitions, one with and the other without RF excitation, following the method outlined in reference [45]. For the single-coil configurations, SNR maps were equivalent to the receive

efficiency, i.e., the receive coil sensitivity divided by the noise image. SNR maps were normalized by the sine of the flip-angle to evaluate the receive-only contribution to the SNR.

Simulations

Numerical simulation software (CST Studio Suite, Darmstadt, Germany) was used to calculate the electromagnetic (EM) field generated by a surface coil or an array of coils in a uniform cylindrical phantom with electrical properties of $\varepsilon_r = 61.8$, $\sigma = 0.87$ S/m, when comparing with the experiments, or $\varepsilon_r = 71$, $\sigma = 0.45$ S/m, for all other cases. Coils were tuned to 297.2 MHz, the proton Larmor frequency at 7T, and matched to 50 Ohms with S_{11} <= −20 dB for each configuration (either without or with HPM (Figs. 1 and 2)) using appropriate matching and tuning capacitors in CST's co-simulator.

For the three-element array, the neighboring elements were geometrically decoupled to obtain S_{21}<=−10dB, as in the experiments. To validate the experiments and determine whether the large HPM pad ($\varepsilon_r = 297$ and $\sigma = 0.38$ S/m) can effectively increase the FOV without penalizing performance, we calculated SNR maps for all coil configurations (Fig. 2). The SNR of the array was calculated by optimally combining the receive sensitivities and dividing the result with a noise covariance matrix [46], derived from the scattering matrix [47], to account for the correlated noise amongst the coil elements. The SNR of a single coil was calculated by dividing the receive sensitivity by the square root of the noise variance, which was calculated using the coil's S_{11}.

We computed $|B_1^+|/\sqrt{P_{diss}}$ (transmit efficiency) and/or $|B_1^-|/\sqrt{P_{diss}}$ (receive efficiency) for various coil-HPM configurations (Fig. 1), where P_{diss} is the dissipated power in the imaging sample that, via reciprocity, is used also as a measure of the noise variance. Transmit efficiency was multiplied with the receive efficiency to determine to what extent they overlapped, with a narrow pattern indicating minimal overlap.

We investigated the effect of positioning an HPM disc at a distance from the coil (Fig. 1B), as well as the effect of shielding the HPM disc with copper (Fig. 1E). Two approaches to partially shield the HPM discs were tested: one where all sides of the HPM disc covered with copper except the surface adjacent to the phantom (copper cap), another with only the lateral surface of the disc covered with copper (copper ring). We compared the results with corresponding cases where HPM was removed leaving only an empty copper cap or a copper ring, in order to isolate the effect of the HPM.

The single coil and HPM (shielded or unshielded) configuration was extended to a four-element array, in which four HPM discs were positioned between adjacent coil elements (Fig. 1C and E). The mean, max and homogeneity (1- (standard deviation/mean)) of the transmit efficiency was calculated for a central axial slice (Fig. 1D).

The performance of the same four-channel array interposed with shielded HPM discs was evaluated with heterogeneous anatomical phantoms of both a smaller head model "Thelonius" (produced from images of a 6 year old boy) [48], and a larger head model "Duke" (produced from images of an adult male) [48] and compared with that of the array

without the HPM discs. For these simulations, the coils' positions were adjusted to closely fit the head model to simulate the performance of dedicated child and adult sized head coils.

Coils in all simulations were modeled with a perfect electrical conductor (PEC). The number of mesh-cells varied from 6 to 25 million depending on the configuration (e.g., single coil with HPM, four-element array with either cylindrical phantom or body model). For all cases, the HPM discs and pads were positioned 2.8 mm away from the phantom to avoid electrical contact and to approximate the thickness of the cylindrical phantom container. Convergence was ensured by setting the accuracy limit <= − 35 dB.

RESULTS

Both simulation and experiments showed that the HPM pad can extend the SNR of the small surface coil over a larger FOV (Fig. 3B vs. 3A and 3F vs. 3E). The resulting SNR was larger than the SNR of a single large coil covering the same FOV (Fig. 3B vs. 3C and 3F vs. 3G), whereas the three-element array outperformed the configuration with the HPM pad (Fig. 3D vs. 3B, and 3H vs. 3F). Note that the phantom properties in Fig. 3 are different (to match the phantom electrical properties used in the experiments) than those of other results (Figs. 4–7), although the phantom dimensions are the same.

A large ideal (i.e., zero conductivity) HPM pad with $\varepsilon_r = 300$ placed below the surface coil extended the transmit and receive sensitivities (Fig. 4D, E vs. A, B). An HPM pad with a higher relative permittivity ($\varepsilon_r = 500$) not only extended the FOV (Fig. 4G and H), but also improved the overlap between the transmit and receive sensitivities (Fig. 4I), as compared to all other cases. A smaller HPM disc ($\varepsilon_r = 300$) placed at 45 degrees with respect to the RF coil (Fig. 1B) also improved the overlap between the transmit and receive sensitivities as compared to a single coil without the HPM disc (Fig. 4L vs. C). For a coil positioned closer to the phantom (0.5 cm above the surface) the transmit and receive efficiency slightly improved at deeper locations (Fig. 4M and N) as compared to the case where the coil was positioned at 2.5 cm from the phantom (Fig. 4A and B). However, the overlap (Fig. 4O) of the transmit and receive sensitivities, as well as the magnitude of the transmit/receive efficiency near the surface did not significantly improve as compared to cases with the HPM pad or disc (Fig. 4I and L).

Figure 5 shows that the spatial distribution of the transmit efficiency varied based on the position of a HPM disc (Fig. 5A and B), with a local enhancement in the field near the position of the HPM disc. However, for an HPM disc with lower relative permittivity ($\varepsilon_r = 80$, Fig. 5C and D) the change in the field distribution was negligible.

Shielding the HPM disc extended the transmit sensitivity of the coil compared to the case without HPM (Fig. 6A vs. Fig. 4A), and changed the transmit field distribution near the position of the HPM disc compared to the case without the shield (Fig. 6A vs. Fig. 5A). In particular, the transmit efficiency was enhanced near the edge of the HPM disc rather than near its center when the shield was added. Using the copper cap (Fig. 6B) or the copper ring (Fig. 6C) alone had a minimal effect on the transmit field distribution within the sample.

In the case of a four-element array, interposing the coils with HPM discs improved transmit efficiency at the periphery of the phantom, but with a reduction at the center by almost 60 % (Fig. 7B vs. Fig. 7A and Table 1). Using copper caps improved transmit efficiency at the center by 13.7 %, without a considerable change at the periphery (Fig. 7C vs. 7A and Table 1). Combining the HPM and the copper caps, i.e., shielded HPM configuration, improved transmit efficiency both at the center (+39 %) and near the surface (Fig. 7D vs. 7A), but did not completely remove the field nulls within the sample (Fig 7D). Table 1 shows that the homogeneity and mean of the transmit efficiency improved the most (59.06 % and 63.6 %, respectively) with the shielded HPM configuration.

Combining HPM discs, either shielded or unshielded, or copper caps without HPM with the four-element array, changed the inductive coupling between the elements from $S_{21}<=-17.7$ dB, when only the coil elements were present, to $S_{21}<=-12.5$ dB for the shielded HPM configuration, $S_{21}<=-14.96$ for the unshielded HPM discs, and $S_{21}<= -17$ dB for the copper caps.

The results for both a child-size head model (“Thelonius”) and larger adult-size head model (“Duke”) showed improvement in transmit efficiency for the configuration with the shielded HPM discs (Fig. 8 and Table 2). The mean transmit efficiency improved the most (20 %) for the smaller head model, whereas transmit homogeneity improved by 38 % for the adult-size head model. However, the performance gain was smaller than for the uniform cylindrical phantom (Table 2 vs. Table 1). The maximum 3D local 10 g SAR decreased for both head models for the configuration with HPM (Thelonius: 2.802 to 2.4 W/kg and Duke: 2.688 to 2.548 W/kg).

DISCUSSION

The distribution of the $\boldsymbol{B}_1$ field within the sample is intrinsically dependent on the operating frequency, electrical properties, size, and shape of the imaging sample [23]. The asymmetric spatial distribution of the $\boldsymbol{B}_1$ fields is increasingly prominent at higher field strengths requiring local transmit coil-arrays, as compared to a large body coil used for transmit at lower field strengths. The FOV of such arrays is generally limited by the array’s physical extent, which depends on the number and size of the individual coil-elements. In this work, we investigated how various configurations of HPM positioned near a surface coil can change the spatial distribution of the transmit and receive sensitivities to increase the FOV and improve imaging efficiency.

The extension in receive sensitivity of a surface coil by placing a large HPM pad between the sample and the coil (Figs. 3 and 4), suggested that HPM could enable the use of arrays with fewer elements to cover a large FOV with high SNR. The results (Fig 3C and B) also indicated that the large HPM does more than effectively increasing the length of the coil conductors, which would have only increased noise susceptibility and decreased SNR. As expected, an optimal combination of three coils covering the same FOV had the highest SNR [46], but at the cost of two additional receive channels. The enhancement in coil performance with HPM of a higher permittivity ($\varepsilon_r = 500$ as compared to $\varepsilon_r = 300$), i.e., extension of the transmit/receive FOV and transmit/receive efficiency (Fig. 4 row 3 vs. row

2), suggested that the use of HPM could be a viable solution when only a few channels are available. This improvement is likely due to the shorter wavelength in the HPM ($\lambda \propto 1/\sqrt{\varepsilon_r}$), resulting in a value of HPM thickness/λ exceeding that of the first cutoff value for a dielectric slab waveguide [49] such that the fields can better propagate along the pad. Additionally, larger displacement currents due to a larger ε_r within the HPM locally enhance the $\boldsymbol{B}_1$ field within the sample.

Mirror asymmetries between transmit and receive sensitivities of a surface coil, particularly prominent at UHF, are caused by eddy currents, which produce a non-uniformity in the spatial distribution of the right (B_1^+) and left (B_1^-) circularly polarized components of the $\boldsymbol{B}_1$ field within the sample [23]. These asymmetries not only produce a field null which adds to the overall $\boldsymbol{B}_1$ inhomogeneity at UHF, but also reduce imaging efficiency due to the poor overlap between B_1^+ and B_1^-, i.e., high excitation and poor receive efficiency (or vice-versa) for the same region. One potential solution is to use separate surface coils for transmit and receive and offset the coil positions to achieve a greater overlap in the sensitivities, which was shown to improve the SNR by around 40 % as compared to using a single transmit/receive coil [50]. Our results suggested that an improvement in imaging efficiency could be achieved with a single transmit-receive coil combined with an HPM pad of appropriate size and relative permittivity (Fig. 4I and L).

To maximize loading and SNR, receive arrays are generally constructed with the individual elements as close as possible to the imaging sample [46]. However, many of the HPM pads used in previous studies were several centimeters thick, which required a substantial gap under the RF coils to accommodate them [24–26]. To test whether the same performance enhancement is possible by removing the HPM and bringing the RF coil closer to the imaging sample, we modeled a surface coil at a distance of 0.5 cm (as opposed to 2.5 cm for all other cases) from the surface of the phantom (Fig. 4M–O). Our results suggested that when transmit and receive sensitivities were normalized by the power dissipated in the phantom, there was a unique advantage in positioning the coil further away from the phantom and using a HPM pad/disc. In fact, the improvement in coil performance in the presence of HPM, with respect to the transmit/receive sensitivity overlap, extension in FOV, and enhancement in magnitude of transit/receive efficiency, especially near the surface of the phantom, was not achieved with a coil (without HPM) positioned closer to the phantom.

A previous optimization study also demonstrated that for a specified spherical sample, when the geometry/position of a HPM disc, coil radius and regions of interest were varied, the combination of HPM and coil always performed better than the coil alone [51]. The same study also noted that there were more degrees of freedom for RF coil design with the HPM than for an RF coil alone [51]. Another study showed that thinner HPM pads with higher relative permittivity performed as well as or even better than thicker HPM pads of a lower relative permittivity, enabling practical incorporation of HPM in tight fitting coil arrays [27].

For all simulated cases, capacitors were used to tune the coils at 297.2 MHz and matched to 50 Ohms. Split resonances in the self-impedance (S_{11}) parameters, which can impede tuning and matching coils [52], were not observed near the operating frequency (data not shown), suggesting that the geometries, electrical properties and position of the HPM pads and discs

did not support resonant modes near the frequency of interest. Therefore, the improvements in the transmit and receive sensitivities observed in the presence of various configurations of HPM are not dependent on specific geometries/electrical properties that support resonant modes.

Although it has been shown that pads with relative permittivity close to water ($\varepsilon_r = 80$) can improve coil performance at high operating frequencies when placed between the coil and the imaging sample [25], we showed that a larger ε_r is needed to manipulate the transmit and receive field patterns when the HPM discs are positioned at a distance from a surface coil (Fig 5). The ability of using HPM to spatially manipulate the transmit and receive fields is likely because of the change in the conservative $\boldsymbol{E}$ fields surrounding the sample. Ordinarily, these conservative $\boldsymbol{E}$ fields do not induce appreciable magnetic fields within the sample that are useful for MRI. However, in the presence of HPM these ambient conservative $\boldsymbol{E}$ fields create significant displacement currents within the HPM, according to the Modified Ampere law, causing a local enhancement in the $\boldsymbol{B}_1$ field within the sample [53].

We partially surrounded HPM discs with a shield with the aim of directing the locally enhanced magnetic field toward the sample. This extended the transmit sensitivity away from coil, and changed its local distribution under the HPM disc (Fig. 6). This effect is the result of combining the partial shield with the HPM disc, and it is not due to the copper layer acting as a passive coil. This is apparent from the fact that using the shield alone (without HPM) or just a copper ring as a passive coil had a negligible effect on the field distribution within the sample.

A value of $\varepsilon_r = 300$ was chosen for the HPM discs in the array (Fig. 7), because that is the highest relative permittivity achievable using a mixture of cheap and readily available materials: Barium titanate powder and deuterium oxide [27,28]. A single coil in conjunction with an HPM disc was chosen as opposed to a coil in conjunction with a large HPM pad, as the latter configuration had a poorer transmit/receive overlap for a relative permittivity of $\varepsilon_r = 300$ (Fig 4). Shielding the HPM discs with copper caps showed the greatest improvement in performance (Table 1). Although very little improvement was observed for a single coil with a copper cap (Fig. 6B), combining four elements with copper caps in phase quadrature may have changed the coupling between the coils and copper caps, resulting in different fundamental field and phase distribution in the imaging sample.

A non-conductive HPM was simulated for the configurations shown in Figs. 4–8 for evaluating the highest possible improvement in transmit and receive efficiencies without any loss (associated with conductivity) in transmitted power or contribution to noise during reception. In practice, however, conformable HPM pads constructed from materials such as a slurry of barium titanate and heavy water (results shown in Fig. 3, simulated with a realistic conductivity of 0.38 S/m) have finite conductivity, which can decrease the coil performance as compared to a lossless HPM. Recent work in manufacturing solid ceramics has enabled the construction of rigid HPM discs with conductivities as low as 0.005 S/m for relative permittivity of around 300 at 297 MHz [54]. Therefore, in practice, with these new ceramics we expect to see very little change with respect to the results shown with lossless HPM. In separate simulations comparing the setup shown in Fig. 7B with and without lossy HPM

discs (ε_r = 300, σ = 0 or 0.005 S/m), we obtained an average percentage difference of 4.6 % for a central transverse plane (data not shown).

For two different sized head models, the four-channel array with shielded HPM discs showed an improvement as compared to the case without HPM (Table 2), but the gain was lower as compared to the case for a cylindrical phantom (Table 1). These results suggest that the effect of HPM on coil performance depends on the size, shape and material properties of the imaging sample. Future work shall aim at optimizing position, size and electrical properties of the shielded HPM discs using heterogeneous body models in the simulations [51,55]. We modeled HPM discs with a relative permittivity of 300 based on practical considerations; however, materials with higher relative permittivity, such as ceramic beads sintered at high temperature mixed with water (ε_r = 500) [28] or ceramic blocks made from lead zirconium titanate (ε_r = 1000)[56,57], could further improve array performance.

Although doubling the number of coils is a feasible alternative, likely resulting in higher performance, to using HPM discs between adjacent coils, practical limits on the number of available transmit channels and the maximum power allowed per channel could still favor the latter option for certain applications. Additionally, reducing the number of channels by increasing the size of individual surface coils would penalize the SNR as shown for an individual coil in Fig 3. However, note that the advantage of using HPM discs, or large HPM pads, to reduce the number of channels and extend the FOV must be balanced with the reduced flexibility for RF shimming and parallel transmit techniques, while broadening coil receive sensitivities could penalize parallel imaging performance.

CONCLUSIONS

Our results demonstrate that the field patterns within the sample can be manipulated based on the size and position of the HPM. In particular, we showed that the SNR of a single surface coil improved over a larger FOV in the presence of a large HPM pad with an appropriate relative permittivity. HPM in conjunction with a surface coil also improved the transmit/receive overlap, suggesting that a single channel with HPM can be used for both transmission and reception with higher imaging efficiency. Interposing partially shielded HPM discs in a four channel array improved the transmit homogeneity in body models, indicating higher coil performance can also be expected in-vivo. Such coil array configurations with HPM discs could be used to reduce the number of channels and minimally sacrifice the SNR performance when using the same array for both transmission and reception.

Acknowledgments

This work was supported in part by NIH R01 EB021277, NIH R01 EB002568, NIH R01 EB011551, NIH R01 EB024536, NSF 1453675, and was performed under the rubric of the Center for Advanced Imaging Innovation and Research (CAI2R, www.cai2r.net), a NIBIB Biomedical Technology Resource Center (NIH P41 EB017183). The authors would like to thank Sebastian Rupprecht for discussions regarding achievable conductivities in ceramic high permittivity materials.

References

1. Vaughan JT, Garwood M, Collins CM, Liu W, DelaBarre L, Adriany G, Andersen P, Merkle H, Goebel R, Smith MB, Ugurbil K. 7T vs. 4T: RF power, homogeneity, and signal-to-noise comparison in head images. Magn Reson Med. 2001; 46(1):24–30. [PubMed: 11443707]
2. Van de Moortele PF, Akgun C, Adriany G, Moeller S, Ritter J, Collins CM, Smith MB, Vaughan JT, Ugurbil K. B(1) destructive interferences and spatial phase patterns at 7 T with a head transceiver array coil. Magn Reson Med. 2005; 54(6):1503–1518. [PubMed: 16270333]
3. Vaughan JT, Snyder CJ, DelaBarre LJ, Bolan PJ, Tian J, Bolinger L, Adriany G, Andersen P, Strupp J, Ugurbil K. Whole-body imaging at 7T: preliminary results. Magn Reson Med. 2009; 61(1):244–248. [PubMed: 19097214]
4. Bomsdorf H, Helzel T, Kunz D, Roschmann P, Tschendel O, Wieland J. Spectroscopy and imaging with a 4 tesla whole-body MR system. NMR Biomed. 1988; 1(3):151–158. [PubMed: 3275125]
5. Barfuss H, Fischer H, Hentschel D, Ladebeck R, Oppelt A, Wittig R, Duerr W, Oppelt R. In vivo magnetic resonance imaging and spectroscopy of humans with a 4 T whole-body magnet. NMR Biomed. 1990; 3(1):31–45. [PubMed: 2390452]
6. Kangarlu A, Baertlein BA, Lee R, Ibrahim T, Yang L, Abduljalil AM, Robitaille PM. Dielectric resonance phenomena in ultra high field MRI. J Comput Assist Tomogr. 1999; 23(6):821–831. [PubMed: 10589554]
7. Ibrahim TS, Lee R, Abduljalil AM, Baertlein BA, Robitaille PM. Dielectric resonances and B(1) field inhomogeneity in UHFMRI: computational analysis and experimental findings. Magn Reson Imaging. 2001; 19(2):219–226. [PubMed: 11358660]
8. Tofts PS. Standing Waves in Uniform Water Phantoms. J Magn Reson Ser B. 1994; 104(2):143–147.
9. Yang QX, Wang J, Zhang X, Collins CM, Smith MB, Liu H, Zhu XH, Vaughan JT, Ugurbil K, Chen W. Analysis of wave behavior in lossy dielectric samples at high field. Magn Reson Med. 2002; 47(5):982–989. [PubMed: 11979578]
10. Collins CM, Liu W, Schreiber W, Yang QX, Smith MB. Central brightening due to constructive interference with, without, and despite dielectric resonance. J Magn Reson Imaging. 2005; 21(2): 192–196. [PubMed: 15666397]
11. Hoult DI, Phil D. Sensitivity and power deposition in a high-field imaging experiment. J Magn Reson Imaging. 2000; 12(1):46–67. [PubMed: 10931564]
12. Ibrahim TS, Lee R, Baertlein BA, Abduljalil AM, Zhu H, Robitaille PML. Effect of RF coil excitation on field inhomogeneity at ultra high fields: A field optimized TEM resonator. Magn Reson Imaging. 2001; 19(10):1339–1347. [PubMed: 11804762]
13. Metzger GJ, Snyder C, Akgun C, Vaughan T, Ugurbil K, Van de Moortele PF. Local B1+ shimming for prostate imaging with transceiver arrays at 7T based on subject-dependent transmit phase measurements. Magn Reson Med. 2008; 59(2):396–409. [PubMed: 18228604]
14. Katscher U, Bornert P, Leussler C, van den Brink JS. Transmit SENSE. Magn Reson Med. 2003; 49(1):144–150. [PubMed: 12509830]
15. Zhu Y. Parallel excitation with an array of transmit coils. Magn Reson Med. 2004; 51(4):775–784. [PubMed: 15065251]
16. Lattanzi R, Sodickson DK, Grant AK, Zhu Y. Electrodynamic constraints on homogeneity and radiofrequency power deposition in multiple coil excitations. Magn Reson Med. 2009; 61(2):315–334. [PubMed: 19165885]
17. Lattanzi R, Wiggins GC, Zhang B, Duan Q, Brown R, Sodickson DK. Approaching ultimate intrinsic signal-to-noise ratio with loop and dipole antennas. Magn Reson Med. 2017; doi: 10.1002/mrm.26803
18. Wiesinger, F., Zanche, ND., Pruessman, KP. Approaching Ultimate SNR with Finite Coil Arrays. Proceedings of the 13th scientific meeting, International Society for Magnetic Resonance in Medicine; Miami. 2005. p. 672
19. Vaidya MV, Sodickson DK, Lattanzi R. Approaching Ultimate Intrinsic SNR in a Uniform Spherical Sample with Finite Arrays of Loop Coils. Concept Magn Reson B. 2014; 44(3):53–65.

20. Wiggins GC, Potthast A, Triantafyllou C, Wiggins CJ, Wald LL. Eight-channel phased array coil and detunable TEM volume coil for 7 T brain imaging. Magn Reson Med. 2005; 54(1):235–240. [PubMed: 15968650]
21. Shajan G, Kozlov M, Hoffmann J, Turner R, Scheffler K, Pohmann R. A 16-channel dual-row transmit array in combination with a 31-element receive array for human brain imaging at 9.4 T. Magn Reson Med. 2014; 71(2):870–879. [PubMed: 23483645]
22. Wardenier, PH. Local Intensity Shift Artifact (LISA). Proceedings of the 8th annual meeting and exhibition, Society of Magnetic Resonance in Medicine; Amsterdam. p. 1175
23. Vaidya MV, Collins CM, Sodickson DK, Brown R, Wiggins GC, Lattanzi R. Dependence of B1+ and B1- Field Patterns of Surface Coils on the Electrical Properties of the Sample and the MR Operating Frequency. Concept Magn Reson B. 2016; 46(1):25–40.
24. Alsop DC, Connick TJ, Mizsei G. A spiral volume coil for improved RF field homogeneity at high static magnetic field strength. Magn Reson Med. 1998; 40(1):49–54. [PubMed: 9660552]
25. Yang QX, Mao W, Wang J, Smith MB, Lei H, Zhang X, Ugurbil K, Chen W. Manipulation of image intensity distribution at 7.0 T: passive RF shimming and focusing with dielectric materials. J Magn Reson Imaging. 2006; 24(1):197–202. [PubMed: 16755543]
26. Haines K, Smith NB, Webb AG. New high dielectric constant materials for tailoring the B1+ distribution at high magnetic fields. J Magn Reson. 2010; 203(2):323–327. [PubMed: 20122862]
27. Teeuwisse WM, Brink WM, Haines KN, Webb AG. Simulations of high permittivity materials for 7 T neuroimaging and evaluation of a new barium titanate-based dielectric. Magn Reson Med. 2012; 67(4):912–918. [PubMed: 22287360]
28. Luo W, Lanagan MT, Sica CT, Ryu Y, Oh S, Ketterman M, Yang QX, Collins CM. Permittivity and performance of dielectric pads with sintered ceramic beads in MRI: early experiments and simulations at 3 T. Magn Reson Med. 2013; 70(1):269–275. [PubMed: 22890908]
29. Webb AG. Dielectric Materials in Magnetic Resonance. Concept Magn Reson A. 2011; 38A(4): 148–184.
30. Yang QX, Wang J, Wang J, Collins CM, Wang C, Smith MB. Reducing SAR and enhancing cerebral signal-to-noise ratio with high permittivity padding at 3 T. Magn Reson Med. 2011; 65(2): 358–362. [PubMed: 21264928]
31. Yang QX, Rupprecht S, Luo W, Sica C, Herse Z, Wang J, Cao Z, Vesek J, Lanagan MT, Carluccio G, Ryu YC, Collins CM. Radiofrequency field enhancement with high dielectric constant (HDC) pads in a receive array coil at 3.0T. J Magn Reson Imaging. 2013; 38(2):435–440. [PubMed: 23293090]
32. Snaar JEM, Teeuwisse WM, Versluis MJ, van Buchem MA, Kan HE, Smith NB, Webb AG. Improvements in high-field localized MRS of the medial temporal lobe in humans using new deformable high-dielectric materials. NMR Biomed. 2011; 24(7):873–879. [PubMed: 21834010]
33. de Heer P, Brink WM, Kooij BJ, Webb AG. Increasing signal homogeneity and image quality in abdominal imaging at 3 T with very high permittivity materials. Magn Reson Med. 2012; 68(4): 1317–1324. [PubMed: 22851426]
34. Brink WM, Webb AG. High permittivity pads reduce specific absorption rate, improve B1 homogeneity, and increase contrast-to-noise ratio for functional cardiac MRI at 3 T. Magn Reson Med. 2014; 71(4):1632–1640. [PubMed: 23661547]
35. Schaller B, Xin L, O'Brien K, Magill AW, Gruetter R. Are glutamate and lactate increases ubiquitous to physiological activation? A 1H functional MR spectroscopy study during motor activation in human brain at 7Tesla. NeuroImage. 2014; 93:138–145. [PubMed: 24555953]
36. Brink WM, van der Jagt AMA, Versluis MJ, Verbist BM, Webb AG. High Permittivity Dielectric Pads Improve High Spatial Resolution Magnetic Resonance Imaging of the Inner Ear at 7 T. Invest Radiol. 2014; 49(5):271–277. [PubMed: 24566290]
37. Lemke C, Hess A, Clare S, Bachtiar V, Stagg C, Jezzard P, Emir U. Two-voxel spectroscopy with dynamic B0 shimming and flip angle adjustment at 7 T in the human motor cortex. NMR Biomed. 2015; 28(7):852–860. [PubMed: 25973740]
38. Lindley MD, Kim D, Morrell G, Heilbrun ME, Storey P, Hanrahan CJ, Lee VS. High-Permittivity Thin Dielectric Padding Improves Fresh Blood Imaging of Femoral Arteries at 3T. Invest Radiol. 2015; 50(2):101–107. [PubMed: 25329606]

39. Manoliu A, Spinner G, Wyss M, Ettlin DA, Nanz D, Kuhn FP, Gallo LM, Andreisek G. Magnetic Resonance Imaging of the Temporomandibular Joint at 7.0 T Using High-Permittivity Dielectric Pads: A Feasibility Study. Invest Radiol. 2015; 50(12):843–849. [PubMed: 26284436]
40. O'Reilly TP, Webb AG, Brink WM. Practical improvements in the design of high permittivity pads for dielectric shimming in neuroimaging at 7T. J Magn Reson. 2016; 270:108–114. [PubMed: 27434779]
41. Neufeld A, Landsberg N, Boag A. Dielectric inserts for sensitivity and RF magnetic field enhancement in NMR volume coils. J Magn Reson. 2009; 200(1):49–55. [PubMed: 19576828]
42. Foo TK, Hayes CE, Kang YW. Reduction of RF penetration effects in high field imaging. Magn Reson Med. 1992; 23(2):287–301. [PubMed: 1549043]
43. Duan Q, Duyn JH, Gudino N, de Zwart JA, van Gelderen P, Sodickson DK, Brown R. Characterization of a dielectric phantom for high-field magnetic resonance imaging applications. Med Phys. 2014; 41(10):102303. [PubMed: 25281973]
44. Klose U. Mapping of the radio frequency magnetic field with a MR snapshot FLASH technique. Med Phys. 1992; 19(4):1099–1104. [PubMed: 1518473]
45. Kellman P, McVeigh ER. Image reconstruction in SNR units: a general method for SNR measurement. Magn Reson Med. 2005; 54(6):1439–1447. [PubMed: 16261576]
46. Roemer PB, Edelstein WA, Hayes CE, Souza SP, Mueller OM. The NMR phased array. Magn Reson Med. 1990; 16(2):192–225. [PubMed: 2266841]
47. Wedge SW, Rutledge DB. Noise waves and passive linear multiports. IEEE Microw Guided Wave Lett. 1991; 1(5):117–119.
48. Christ A, Kainz W, Hahn EG, Honegger K, Zefferer M, Neufeld E, Rascher W, Janka R, Bautz W, Chen J, Kiefer B, Schmitt P, Hollenbach HP, Shen J, Oberle M, Szczerba D, Kam A, Guag JW, Kuster N. The Virtual Family--development of surface-based anatomical models of two adults and two children for dosimetric simulations. Phys Med Biol. 2010; 55(2):N23–38. [PubMed: 20019402]
49. Yariv, A. Optical Electronics. 4. Oxford University Press; USA: 1995.
50. Wiggins, GC., Duan, Q., Lattanzi, R., Sodickson, DK. B1+ and SNR Optimization of High Field RF Coils Through Offsetting of Transmit and Receive Elements. Proceedings of the 17th scientific meeting, International Society for Magnetic Resonance in Medicine; Honolulu. 2009. p. 2951
51. Luo, W., Qing, Y., Collins, CM. Improved surface coil performance at any depth in a lossy sphere with a dielectric disc. Proceedings of the 22nd scientific meeting, International Society for Magnetic Resonance in Medicine; Milan. 2014. p. 4812
52. Haemer, GG., Collins, CM., Sodickson, DK., Wiggins, GC. Discovering and working around effects of unwanted resonant modes in high permittivity materials placed near RF coils. Proceedings of the 23rd scientific meeting, International Society for Magnetic Resonance in Medicine; Toronto. 2015. p. 0859
53. Collins, CM., Carluccio, G., Vaidya, MV., Haemer, G., Luo, W., Lattanzi, R., Wiggins, GC., Sodickson, DK., Yang, QX. High-permittivity Materials can Improve Global Performance and Safety of Close-Fitting Arrays. Proceedings of the 22nd scientific meeting, International Society for Magnetic Resonance in Medicine; Milan. 2014. p. 0404
54. Rupprecht, S. personal communication. Jul 31, 2017
55. Lattanzi, R., Vaidya, MV., Carluccio, G., Sodickson, DK., Collins, CM. Effects of high-permittivity materials on absolute RF coil performance as a function of B0 and object size. Proceedings of the 22nd scientific meeting, International Society for Magnetic Resonance in Medicine; Milan. 2014. p. 4818
56. Sica, C., Luo, W., Rupprecht, S., Lanagan, M., Collins, CM., Sahul, R., Kwon, S., Yang, Q. Ultra High Dielectric Constant (uHDC) Head Insert at 3T for Dramatic Reduction of SAR and B1+ inhomogeneity. Proceedings of the 22nd scientific meeting, International Society for Magnetic Resonance in Medicine; Milan. 2014. p. 0405
57. Koolstra K, Börnert P, Brink W, Webb A. Improved image quality and reduced power deposition in the spine at 3 T using extremely high permittivity materials. Magn Reson Med. 2017; doi: 10.1002/mrm.26721

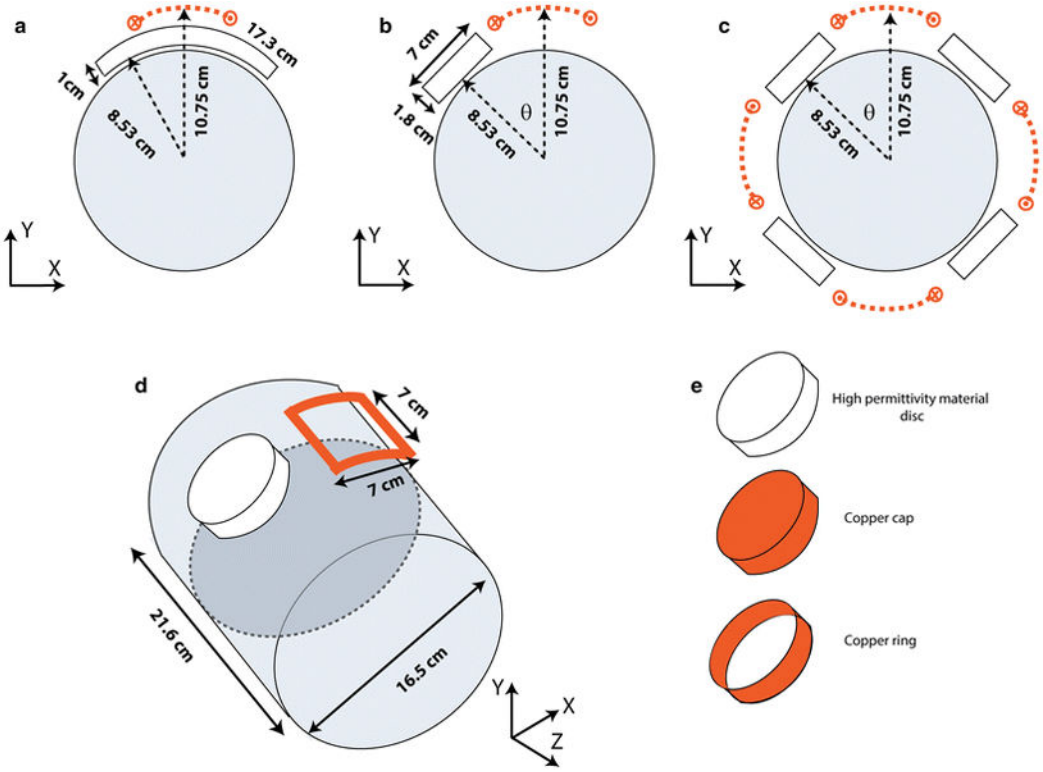

Figure 1.

Schematic representations of the various simulation setups, including a cylindrical phantom (gray), loop coils (orange) and HPM pads (white). The EM field was calculated for a transverse plane through the center of the coil, which was positioned 2.5 cm above the surface of the phantom. Both the large HPM pad (A) and the HPM disc (B, C) were modeled at 2.8 mm from the surface of the phantom. Different values for the angle (θ) between the HPM disc and the center of the coil were tested. The 3D geometry of the simulation setup and the central transverse plane (dark gray) used to evaluate the fields is shown in D. In E the HPM disc is shown together with the copper cap and copper ring, which were modeled for some of the simulations. The shielded HPM disc (not shown) was made by combining the HPM disc and the copper cap. Phantom properties were $\varepsilon_r = 61.8$ and $\sigma = 0.87$ S/m for Fig. 3 and $\varepsilon_r = 71$, $\sigma = 0.45$ S/m for Figs. 4–7.

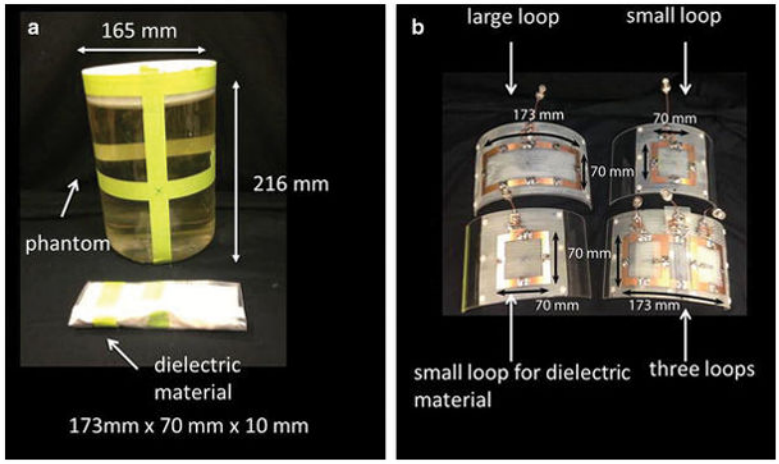

Figure 2.

RF coils, HPM pad and phantom used for the experiments. Phantom (ε_r = 61.8 and σ = 0.87 S/m) and HPM (ε_r = 297, σ = 0.38 S/m) dimensions are shown in (A). All coil configurations are shown in (B). Coils were tuned and matched at 297.2 MHz. The small loop for dielectric material was tuned and matched in conjunction with the HPM material. The coils were positioned at a distance of 2.5 cm from the phantom in all cases.

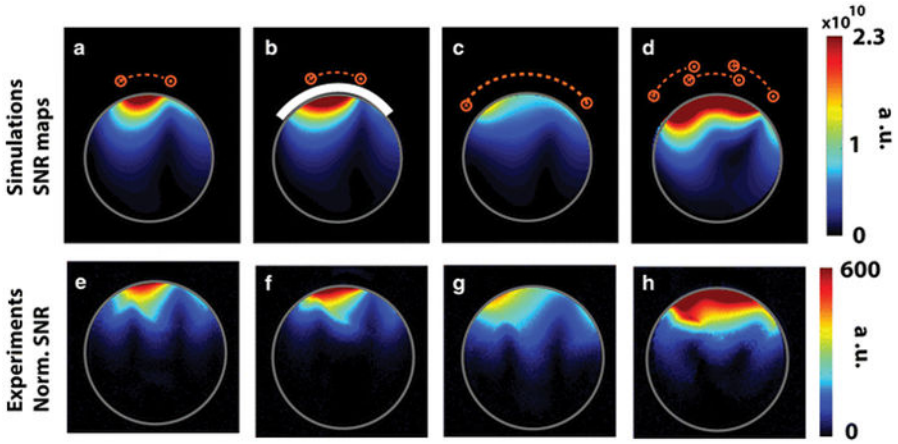

Figure 3.

Experimental and simulated SNR maps for the geometries in Fig. 2B. Experimental SNR maps were normalized by the sine of the flip angle to show only receive contribution, which resulted in artifacts when dividing by low flip angle values. Experimental SNR maps and simulated SNR maps show the same trend and are in good agreement with each other. The configuration with a large HPM pad (white) under the coil (B and F) performed better than a single large coil (C and G) and had a wider sensitivity profile than a single surface coil (A and E), but was outperformed by the three-coil array (D and H). Sample properties used in both simulation and experiment were $\varepsilon_r = 61.8$ and $\sigma = 0.87$ S/m for the phantom and $\varepsilon_r = 297$ and $\sigma = 0.38$ S/m for the HPM pad.

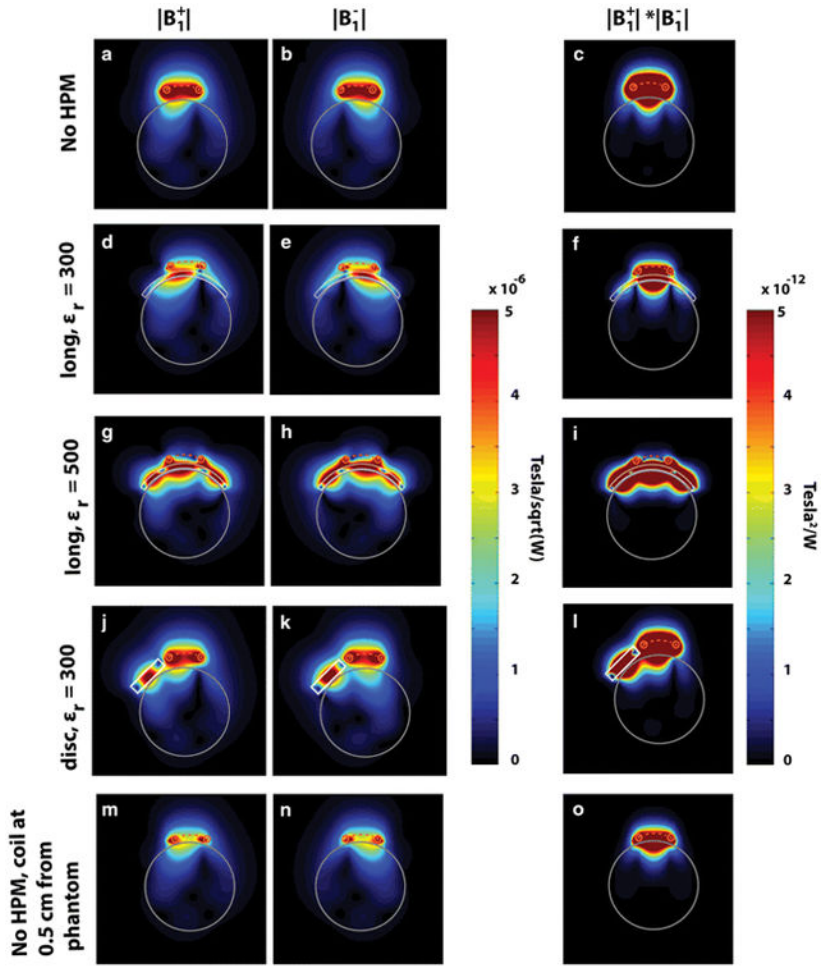

Figure 4.

Effect of various HPM configurations on the transmit ($|B_1^+|$) and receive ($|B_1^-|$) sensitivities, and total overlap between the two ($|B_1^+|*|B_1^-|$) at 7T. $|B_1^+|$ and $|B_1^-|$ exhibit mirror asymmetries (A and B) and overlap over a small central region (C) in the absence of a HPM disc. A large HPM pad with $\varepsilon_r = 300$ (D–F) extend the sensitivities over a wider region (D, E vs. A, B). Increasing the relative permittivity of the HPM pad to $\varepsilon_r = 500$ (G–I) extends the coil FOV and reduces the asymmetry between transmit field and receive sensitivity further improving their overlap (I). In the presence of an HPM disc (J–L), the $|B_1^+|$ and $|B_1^-|$ patterns are still asymmetric, but overlap over a larger region than for the cases A–F. Moving the coil closer to the phantom (M–O) did not significantly improve the overlap (O vs. I, L), or improve the magnitude of the transmit (M vs. A) and receive sensitivity (N vs. B) near the surface. Note that transmit field and receive sensitivity maps were normalized by the dissipated power in the phantom for all cases.

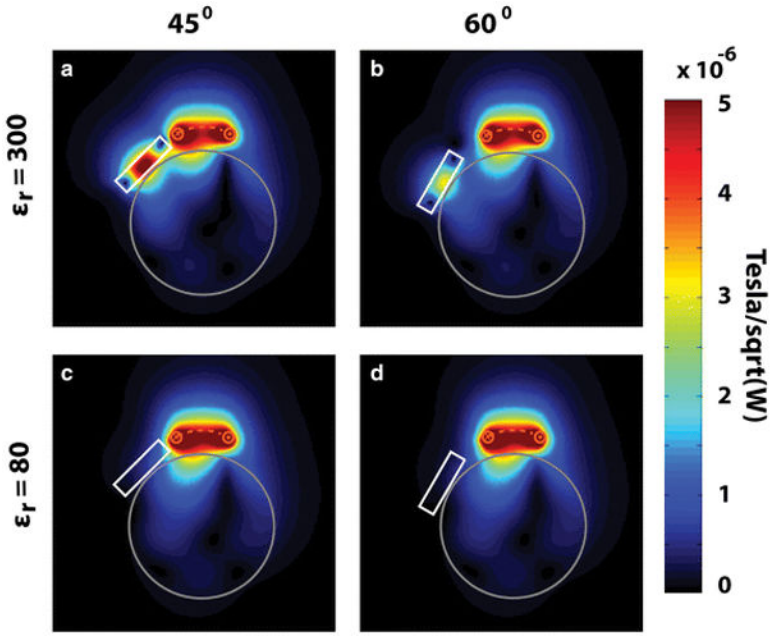

Figure 5.

The effect of changing the position of the HPM disc (white) with respect to the coil (orange) on the transmit efficiency. For an HPM disc with relative permittivity of 300 (A and B), the spatial distribution of the transmit efficiency changed based on the position of the disc. For a disc with lower relative permittivity (C and D), the effect was minimal.

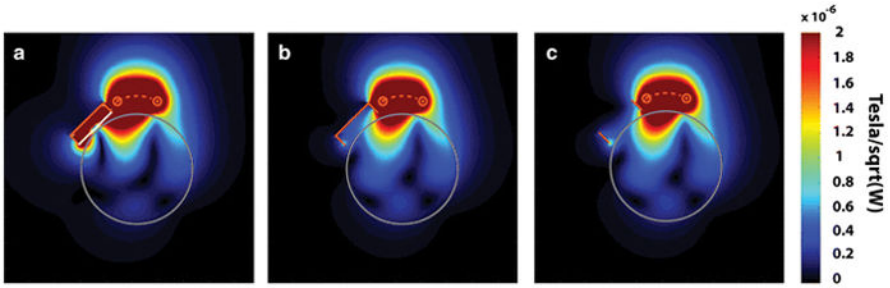

Figure 6.

The effect of partially shielding the HPM disc on the transmit efficiency. For a disc of HPM (ε_r =300) shielded with copper (A), field distribution extends towards the shielded HPM. Removing the HPM from the shielded disc (B), i.e., leaving an empty copper cap, or replacing the shielded disc with a copper ring with only the lateral copper surface present (C), resulted in no distinguishable change in the transmit field distribution compared to the coil-only case (Fig. 4A). Note that the maximum of the colorscale is different from Fig. 4 in order to visualize small changes in the field distribution near the copper cap and copper ring.

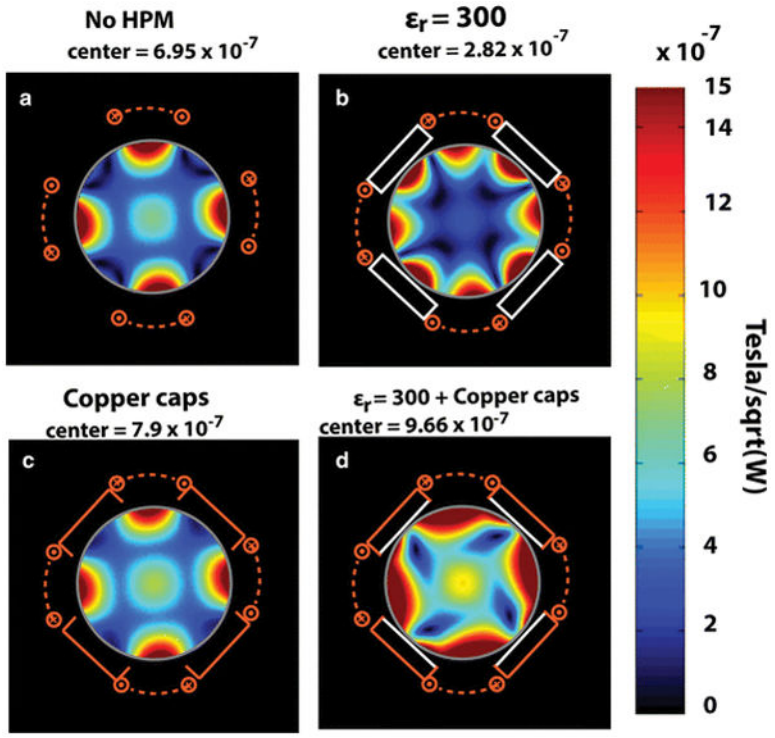

Figure 7.

Transmit efficiency for different four-element array designs. Coils were driven in quadrature in each case. HPM discs interposed between adjacent coils (B) enhanced the transmit efficiency locally, near the position of the HPM discs, but decreased the transmit efficiency at the center. Copper caps alone (C) improved the transmit efficiency at the center. Copper caps with HPM (D), improved transmit efficiency overall, except in small regions below the discs.

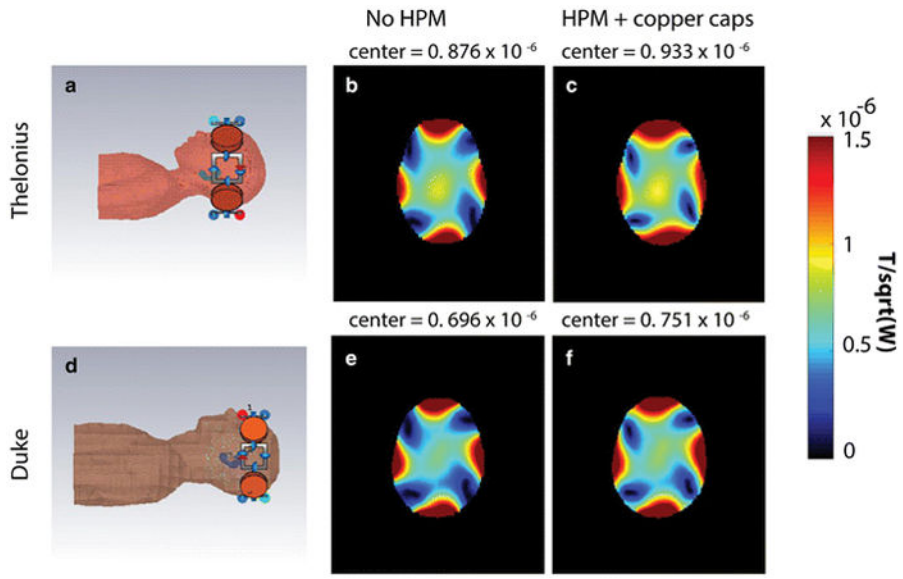

Figure 8.

Transmit efficiency maps for a central transverse slice for head models of different sizes (A and D). Transmit efficiency improved overall in the presence of shielded HPM discs (C and F), although the improvements were smaller than those observed in the case of a symmetrical homogeneous cylindrical phantom (Fig. 7). Note that the position of the coils and HPM discs were slightly modified as compared to the arrangement for a cylindrical phantom to account for the shape and size of the head models.

Table 1

Percentage change in transmit efficiency for HPM and cap configurations shown in Fig. 7B–D with respect to no HPM (Fig 7A)

	center	mean	max	homogeneity
HPM discs	−59.44	11.76	49.23	−43.12
Copper caps	13.72	8.64	−7.63	52.86
HPM + Copper caps	38.99	63.60	14.65	59.06

Table 2

Percentage change in performance when the 4-element array is combined with HPM disc and cap (Fig. 8C and F) with respect to the case without HPM (Fig. 8B and E).

	Transmit Efficiency			B1+ uniformity	Max 3D local 10g SAR for constant input power
	center	mean	max		
Thelonius (child)	6.5	19.94	6.71	15.63	−14.35
Duke (adult)	7.93	11.36	−9.86	37.59	−5.21